Supplementary Materials for

Bridging Bound States in the Continuum and Coherent Perfect Absorption via Dynamic Singularity Engineering

Hang Liu[1], Lei Wang[1], Junwei Liu[1], Haizhi Ni[1], Caihong Zhang[1,2], Jingbo Wu[1,2], Jian Chen[1,2], Huabing Wang[1,2], Xianshun Ming[3], Biaobing Jin[1,2], Peiheng Wu[1,2] and Kebin Fan[1,2*]

[1]*Research Institute of Superconductor Electronics (RISE), School of Electronic Science and Engineering, Nanjing University, Nanjing 210093, China*

[2]*Purple Mountain Laboratories, Nanjing 211111, China*

[3]*State Key Laboratory of Ultrafast Optical Science and Technology, Xian Institute of Optics and Precision Mechanics, Chinese Academy of Sciences, Xian 710119, China*

Correspondence should be addressed to: kebin.fan@nju.edu.cn

Section 1. Temporal Coupled Mode Theory (TCMT) Model and Construction for the Metasurfaces

The designed metasurface is fabricated by sputtering a gold film on the bottom surface of a sapphire substrate (relative permittivity $\varepsilon_1 = 9$) and structuring gold (conductivity $\sigma_{\mathrm{Au}} = 4.561 \times 10^7$ S/m) and VO_2 (relative permittivity $\varepsilon_2 = 9$, conductivity approximating 0 at room temperature) on the top surface to form a periodic THz metasurface array. The bottom gold film (thickness $h_0 = 200$ nm) acts as a total reflection mirror, exceeding the skin depth of gold at the operating frequency. The top structure consists of a pair of periodic short-armed U-shaped resonators, which are mirror-symmetric. Their period $P = 121$ μm, line width $w = 22.5$ μm, resonator spacing $g = 25$ μm, long arm $l = 80$ μm. Each two adjacent resonators are bridged by VO_2 with width $w_1 = 20$ μm. It is worth noting that when VO_2 is in the dielectric state, its dielectric properties are almost identical to those of sapphire, with only a 0.2 μm height difference in geometric dimensions, which has no effect on the original mode types and distributions. This typical metal-insulator-metal structure fixes the function of energy exchange through a single port of the system due to zero transmission. The optical evolution process involves interactions between two modes and one port. Therefore, the system can be described by TCMT[1] as follows:

$$\begin{cases} \dfrac{da}{dt} = -i(\Omega - i\Gamma)a + K^T S_+ \\ S_- = CS_+ + Da \end{cases} \tag{S1}$$

Assuming a single-mode system, the intrinsic properties of the mode are defined by its resonance frequency $\Omega = \omega_0$ and total loss $\Gamma = \gamma_r + \gamma_d$, accounting for both radiative (γ_r) and dissipative (γ_d) damping. The coupling strength between the mode and the radiation port is dictated by $|D|^2 = 2\gamma_r$. Accordingly, the scattering matrix S takes the following form:

$$\begin{aligned} S &= C + iD\left[\omega + (-\Omega + i\Gamma)\right]^{-1} D^T \\ &= C\left\{1 - iD^*\left[\omega + (-\Omega + i\Gamma)\right]^{-1} D^T\right\} \\ &= C\left\{\frac{\omega - \left[\omega_0 + i\left(\gamma_r - \gamma_d\right)\right]}{\omega - \left[\omega_0 - i\left(\gamma_r + \gamma_d\right)\right]}\right\}, \end{aligned} \tag{S2}$$

The zero and pole of the S-matrix are defined as $\omega_z = \omega_0 + i(\gamma_r - \gamma_d)$ and $\omega_p = \omega_0 - i(\gamma_r + \gamma_d)$, respectively. In a pristine Hermitian system where no energy exchange occurs ($\gamma_r = \gamma_d = 0$), BIC is characterized by $\omega_z = \omega_p = \omega_0$, indicating that the zero and pole are complex conjugates that coalesce exactly on the real frequency axis. In a non-Hermitian system devoid of dissipative (Ohmic) loss ($\gamma_r \neq 0, \gamma_d = 0$), the coordinates evolve to $\omega_z = \omega_0 + i\gamma_r$ and $\omega_p = \omega_0 - i\gamma_r$. In this regime, the zero and pole maintain their complex-conjugate symmetry for both BIC ($\gamma_r = 0$) and QBIC. In contrast, for a Hermitian system incorporating dissipative loss ($\gamma_r = 0, \gamma_d \neq 0$), the relations become $\omega_z = \omega_p = \omega_0 - i\gamma_d$. Here, the zero and pole of the BIC

deviate from the real axis and shift into the lower half of the complex frequency plane while remaining coalesced. Our investigation focuses on non-Hermitian systems with intrinsic dissipative losses. Under these conditions, the introduction of radiative loss causes the zero and pole of the QBIC to bifurcate. Specifically, the QBIC zero resides in the upper half-plane only when the radiative rate exceeds the dissipation rate ($\gamma_r > \gamma_d$). At the critical condition $\gamma_r = \gamma_d$, the zero returns to the real axis; however, the corresponding pole remains situated in the lower half-plane, distinguishing this state from a lossless BIC. When $\gamma_r < \gamma_d$, both the zero and the pole fall into the lower half-plane, where the trajectory of the pole dictates the evolution of the QBIC Q factor.

For a dual-mode system, $a = \begin{pmatrix} a_1 \\ a_2 \end{pmatrix}$ and the effective Hamiltonian is given by:

$$H_{eff} = \Omega - i\Gamma = \begin{bmatrix} \omega_1 - i(\gamma_1 + \gamma_{d1}) & \kappa_1 + i\kappa_2 \\ \kappa_1 + i\kappa_2 & \omega_2 - i(\gamma_2 + \gamma_{d2}) \end{bmatrix} \tag{S3}$$

here, ω_j denotes the frequency of the j-th mode, while κ_1 represents the coherent coupling coefficient between mode 1 and mode 2. The parameters γ_j and γ_{dj} correspond to the radiative and dissipative losses of the j-th mode, respectively. Additionally, κ_2 represents the dissipative coupling coefficient between the two modes. S_+ is the incident port, and S_- is the output port. $K = D$ is the coupling between the modes and the ports, and C is the background direct scattering matrix. Here, we consider the asymmetric phase of the evanescent wave decaying towards the ports, that is, $D = \begin{pmatrix} D_{11} & D_{12} \end{pmatrix} = \begin{pmatrix} d_{11}e^{-i\alpha} & d_{12}e^{-i\beta} \end{pmatrix}$, and d_{kj} is the coupling between the incident port k and the mode j. Meanwhile, we assume that the phase between port 1 and mode 1 is α, and the phase between port 1 and mode 2 is β. It is worth noting that in the above description, we all use j to represent the mode and k to represent the port.

In the absence of resonance, the incident wave acquires additional phase upon traversing the metasurface; therefore, we define the background scattering matrix as $C = -e^{-i\theta}$. The unique architecture of the metasurface enables the Fabry-Pérot (FP) mode to propagate within the dielectric spacer, reflect off the gold mirror, and subsequently couple with the QBIC mode co-located in the top layer of the metasurface.

Variations in the dielectric thickness induce a phase retardation, thereby introducing a phase difference into the inter-mode complex coupling term $\tilde{\kappa}$ within the TCMT framework. This phase shift not only determines the coherent coupling strength κ_1 but also induces a dissipative coupling component κ_2, which incorporates the far-field coupling term $i\sqrt{\gamma_1\gamma_2}$, yielding the total complex coupling $\tilde{\kappa} = \kappa_1 + i\kappa_2$. Therefore, the reflection coefficient of the coupled system can be derived as follows:

$$\begin{aligned} r(\omega) &= C + iD[\omega I + (-\Omega + i\Gamma)]^{-1}D^T \\ &= C\big(1 - iD^*[\omega I + (-\Omega + i\Gamma)]^{-1}D^T\big) \\ &= -e^{-i\theta}\left[1 - i\frac{D_{11}^2\Delta_2 + D_{12}^2\Delta_1 + 2\tilde{\kappa}D_{12}D_{11}}{\Delta_1\Delta_2 - \tilde{\kappa}^2}\right] \end{aligned} \tag{S4}$$

Where $\Delta_1 = \omega - \omega_1 + i(\gamma_1 + \gamma_{d1})$ and $\Delta_2 = \omega - \omega_2 + i(\gamma_2 + \gamma_{d2})$. The system obeys the law of energy conservation, i.e., $D^+D = 2\Gamma_r$, where Γ_r denotes the radiation loss. We set $\tau = \alpha - \beta$. Since the system additionally satisfies $CD^* = -D$, calculations yield $\tau = 0$ or $\pm\pi$. In this study, we primarily utilize $\tau = \pm\pi$ to derive the spectral formula and elucidate the mechanisms of mode loss and mode coupling, with $|D_{11}| = \sqrt{2\gamma_1}, |D_{12}| = \sqrt{2\gamma_2}$, and $D_{11}D_{12} = -2\sqrt{\gamma_1\gamma_2}$.

To determine the coupling conditions for CPA using TCMT, we apply the concept of scattering zeros. The zeros are identified when the eigenvalue of the scattering matrix $r(\omega)$ vanishes. The resulting expression for the eigenfrequencies is given by:

$$\begin{aligned}\omega_{z1,z2} = &\frac{\omega_2 + \omega_1}{2} - i\frac{(\gamma_{d1} - \gamma_1) - (\gamma_2 - \gamma_{d2})}{2} \\ &\pm \frac{1}{2}\sqrt{\left[(\omega_1 - \omega_2) - i(\gamma_{d1} - \gamma_1 + \gamma_2 - \gamma_{d2})\right]^2 + 4[\kappa_1 + i(\kappa_2 - 2\sqrt{\gamma_1\gamma_2})]^2}\end{aligned} \tag{S5}$$

Additionally, by solving for the eigenvalues (poles) of the system's effective Hamiltonian (S3), the eigenfrequencies of the modes are derived as:

$$\begin{aligned}\omega_{p1,p2} = &\frac{\omega_1 + \omega_2}{2} - i\frac{\gamma_1 + \gamma_{d1} + \gamma_2 + \gamma_{d2}}{2} \\ &\pm \frac{1}{2}\sqrt{[\omega_1 - \omega_2 + i(\gamma_2 + \gamma_{d2} - \gamma_1 - \gamma_{d1})]^2 + 4\left(\kappa_1 + i\kappa_2\right)^2}\end{aligned} \tag{S6}$$

It is essential to characterize the coupling between the BICs and FP modes using the eigenfrequencies derived above. Moreover, the variation of the Q-factor during the degradation of the BIC mode can be elucidated by analyzing the dissipative terms within these eigenfrequencies.

When $\omega_1 = \omega_2 = \omega_0$ and the CPA condition ($\mathrm{Im}(\omega_{z2}) = 0$) is satisfied, the coupling condition can be defined as:

$$\begin{cases}\kappa_1 = \sqrt{(\gamma_{d1} - \gamma_1)(\gamma_2 - \gamma_{d2})} \\ \kappa_2 = 2\sqrt{\gamma_1\gamma_2}\end{cases} \tag{S7}$$

By substituting the CPA conditions into the eigenfrequencies of the zeros ω_{z1} and ω_{z2}, the expressions reduces to:

$$\begin{cases}\omega_{z1} = \omega_0 - i(\gamma_{d1} - \gamma_1 - \gamma_2 + \gamma_{d2}) \\ \omega_{z2} = \omega_0.\end{cases} \tag{S8}$$

Interestingly, in addition to one of the two zeros being located on the real axis, their real parts are identical. Furthermore, the absorptivity of the resonant system for THz waves is formulated as:

$$A(\omega) = 1 - r^2(\omega) \tag{S9}$$

Section 2. Analysis of Band Folding Phenomenon

By directly observing the band distributions under different reciprocal lattice vector periods, we elaborate on the process of band folding in the Brillouin zone. Fig. 1a shows the blue band distribution under a small period ($P = a$) in the x-direction, displaying only half a period, with the corresponding reciprocal lattice vector period being $2\pi/a$. When a perturbation is introduced into the metasurface, the small period abruptly transitions to a large period ($P = 2a$), and the reciprocal lattice vector period becomes π/a. The bands existing in Fig. 1a continue to persist, while translated red bands appear in reciprocal space due to the system's periodicity. Meanwhile, due to the mirror symmetry of the metasurface geometry about the Γ point and wave vector symmetry, the energy is symmetric about $k_x = 0$, as shown by the green line in Fig. 1b. Here, we only plot the band distribution after folding for $k_x \in [0, \pi/2a]$, such that the energy points originally at the X point of the blue line exhibit folding behavior[2] at the Γ point of the green line.

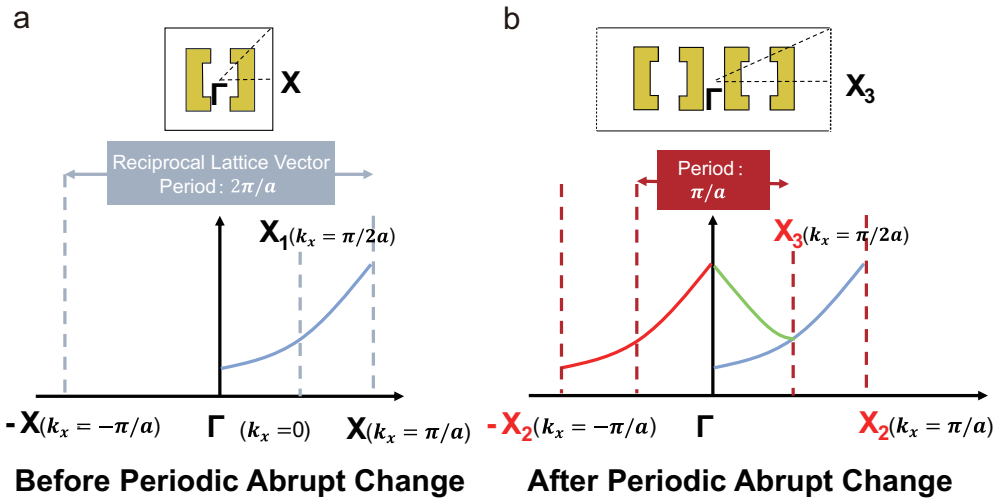

Fig. 1 Band folding phenomenon induced by abrupt periodicity change in real space. **(a)** Before the abrupt change. **(b)** After the abrupt change.

Section 3. Physical phenomena arising from the manipulation of poles and zeros

As illustrated in Fig. 2a, manipulating the complex poles of the BIC is achieved by dynamically tuning the VO_2 conductivity (σ) at a period of P. As described in Fig. 1d of the main text, increasing the VO_2 conductivity ($\sigma \uparrow$) drives a reconfigurable evolution from a folded BIC state to a folded QBIC state. Specifically, at frequency ω_2, the BIC mode transitions from an invisible state to a lossy QBIC mode with distinct resonance features. This transition introduces a radiative loss element (γ_1) and

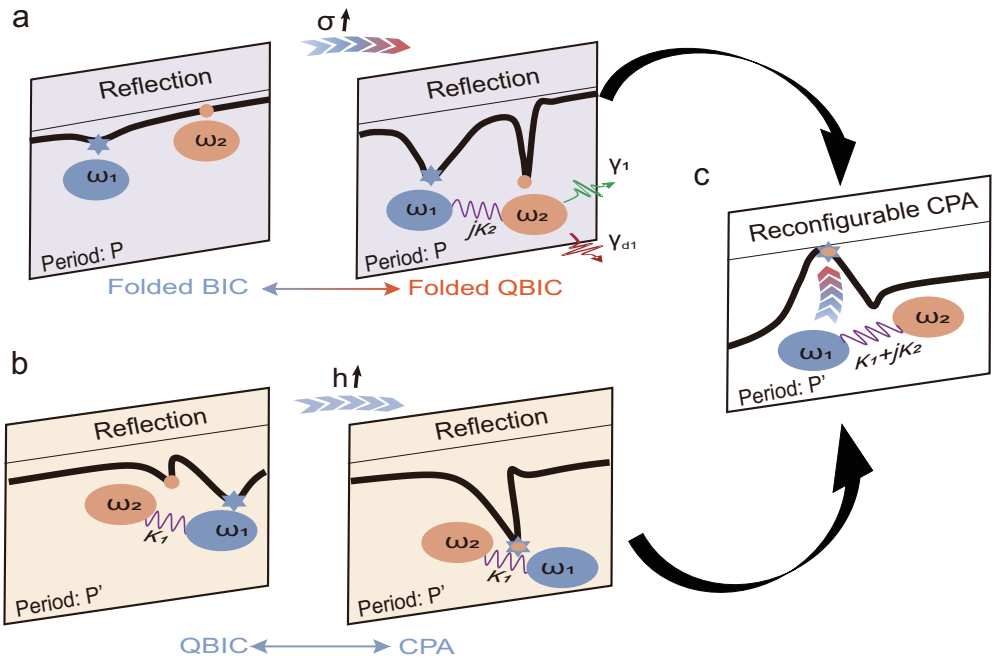

Fig. 2 Physical phenomena arising from the manipulation of zeros and poles. The blue and orange markers correspond to the FP mode and BIC, respectively.(a) Schematic of the dynamic modulation process from a folded BIC to a folded QBIC. **(b)** Transition from QBIC to CPA. **(c)** Realization of reconfigurable CPA.

a dissipative loss element (γ_{d1}). Driven by this dissipation mechanism, a pronounced dissipative coupling($i\kappa_2$) emerges between the FP mode (ω_1) and the QBIC mode (ω_2).

Figure 2b demonstrates the manipulation of the complex zeros of the BIC by varying the metasurface substrate thickness (h) at a different period P', while keeping σ_{VO_2} fixed at the QBIC state. As the substrate thickness increases ($h \uparrow$) or decreases ($h \downarrow$), the complex zeros of the system are steered back to the real axis. Concurrently, the real coherent coupling (κ_1) between the modes becomes prominent. Owing to the strong inter-mode coupling, the matching of the zero on the real axis, and the significant optical interference effects induced by the FP cavity, a perfect zero is realized in the reflection spectrum when the mode frequencies match ($\omega_1 \approx \omega_2$), yielding the CPA phenomenon.

Finally, Fig. 2c summarizes the independent zero and pole manipulation mechanisms revealed above. By leveraging two degrees of freedom at period P'—conductivity tuning to introduce $i\kappa_2$ and substrate thickness tuning to introduce κ_1—a reconfigurable CPA with complex coupling ($\kappa_1 + i\kappa_2$) is achieved. This corresponds to the physical phenomena described in the main text, where zeros or poles are manipulated via transverse or longitudinal shifts driven by independent parameters. Consequently, the CPA response can be dynamically reconfigured by further tuning σ_{VO_2}.

Section 4. FP modes in metasurfaces

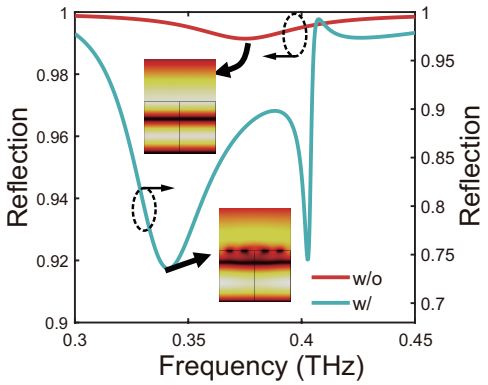

Fig. 3 FP mode spectra and yz-plane electric field distributions for the patterned and unpatterned metasurfaces. The thickness for both cases is $h_1 = 200$ μm, with the VO_2 conductivity of the patterned sample set to $\sigma_{VO_2} = 9.2 \times 10^4$ S/m.

It should be noted that the FP mode propagates in the dielectric layer, is reflected back at the gold mirror, and undergoes co-located coupling with the QBIC mode in the metasurface structure layer. Varying the dielectric thickness leads to distinct phase delays and overall coupling strengths. Within the framework of TCMT, this is denoted by the complex inter-mode coupling term $\kappa e^{-i\phi}$, which can be explicitly decomposed into the coherent coupling strength κ_1 and the dissipative coupling κ_2 between the interacting modes.

For a metasurface with the topmost structure removed, the corresponding electromagnetic spectrum is depicted by the red curve in Fig. 3; the inset illustrates the electric field distribution of the FP mode in the yz-plane at 0.375 THz. It can be observed that upon incidence into the dielectric layer, the electric field alters its propagation direction and, following reflection by the bottom gold mirror, propagates along the $+z$-direction. In the presence of our fully designed structure ($h_1 = 200$ μm), the yz-plane electric field distribution of the low-frequency FP mode, corresponding to the blue curve (0.3411 THz), exhibits a profile similar to that of the unstructured case. The primary distinction lies in the increased material loss introduced by the top structure, which is manifested in the spectrum.

Section 5. Electric Field Distribution during BIC Evolution

In this section, Fig. 4a illustrates that as the conductivity increases, the VO_2 region acts as an enhanced perturbation, transforming the BIC mode into a QBIC. During this process, the energy field gradually diffuses toward the VO_2 cut-wires, enabling the VO_2 cut-wires to participate in the mode distribution. This further enhances

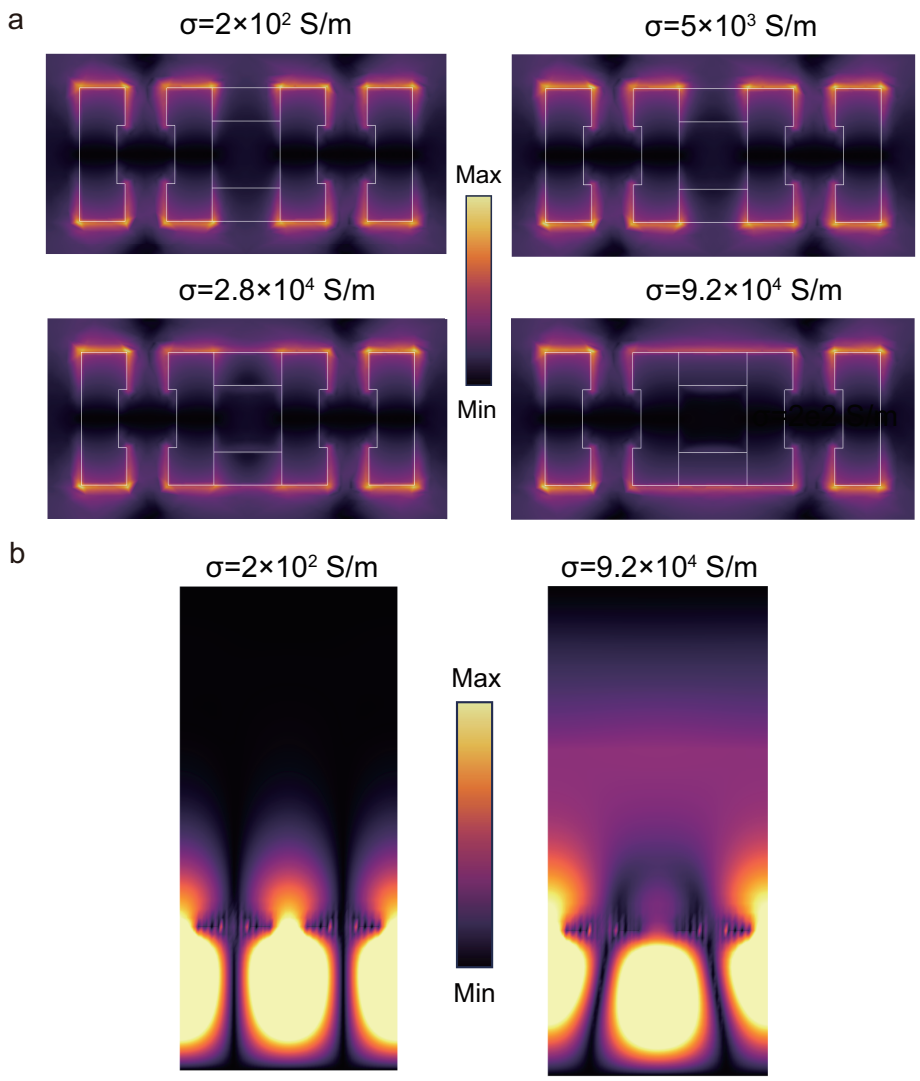

Fig. 4 **(a)**Electric field distribution in the xy plane as a function of conductivity. **(b)** Radiated electric field distributions in the xz plane for BIC and QBIC.

the perturbation effect on the BIC mode to increase loss. Fig. 4b shows the electric field distributions in the x-z plane under different conductivities. In the absence of perturbation or with extremely small perturbation, the far-field radiation of the BIC mode is not observable, whereas the far-field radiation of the QBIC degenerated by increased conductivity is remarkably distinct.

Section 6. Spectral Verification of Folded BICs in Active THz Metasurface Systems

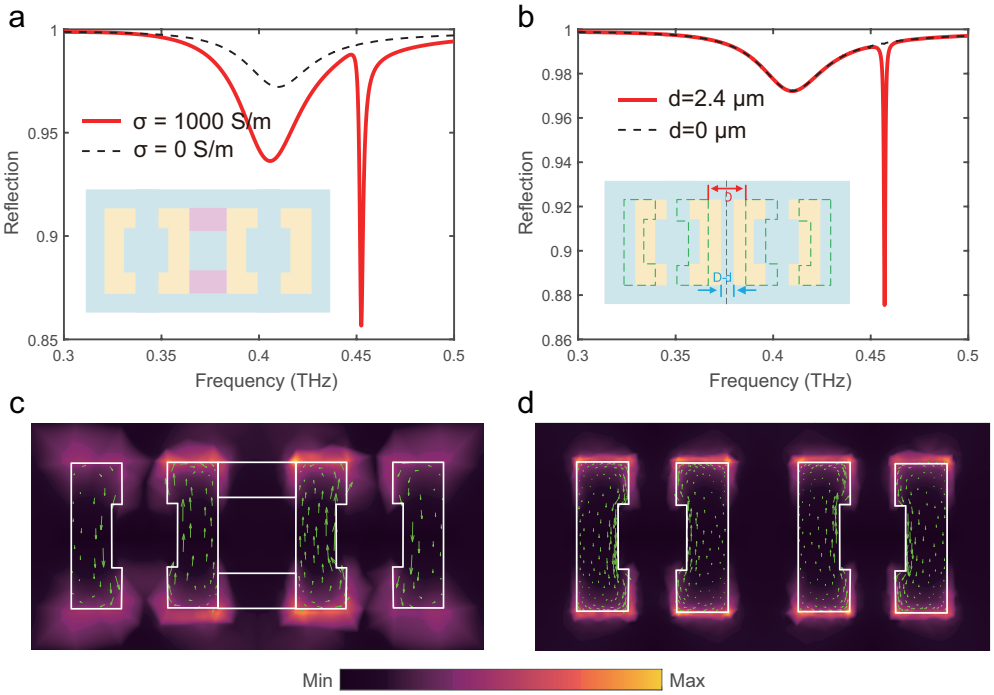

Fig. 5 **(a)** x-y plan view of the proposed perturbed metasurface and the corresponding spectrum of the folded QBIC mode. **(b)** x-y plan view of the conventional perturbed metasurface and the corresponding spectrum of the folded QBIC mode. **(c)** Electric field and current distributions in the x-y plane for the active tuning system. **(d)** Electric field and current distributions in the x-y plane for the passive control system.

Here, by comparing QBICs generated via two methods of introducing system perturbations, Fig. 5a shows that gap perturbation in the passive system leads to the emergence of QBIC modes, while Fig. 5b depicts the designed THz metasurface in this work. Figs. 5c and 5d present the electric field distributions of Figs. 5a and 5b respectively, where green arrows indicate the current distributions under the two QBIC modes. Under perturbation, the current in the active system flows along the outer side of the U-shaped ring, opposite to that on the mirror-symmetric side, which is consistent with the passive system. This confirms the same origin of the two QBIC modes from another perspective and verifies the feasibility of the designed system through spectral characteristics and current distributions.

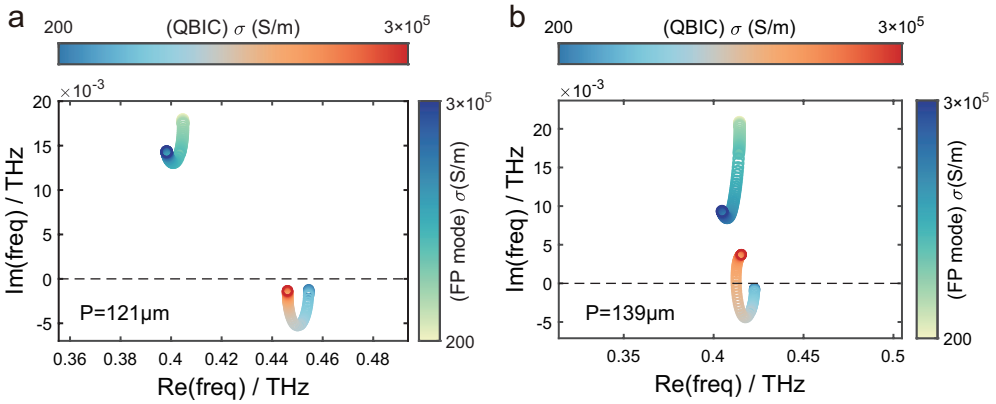

Fig. 6 **(a), (b)** show the zeros shift of the BIC and FP modes induced by conductivity variations at $P = 121$ μm and $P = 139$ μm, respectively.

Section 7. Evolution of zeros

As shown in Figs. 6a and b, with increasing conductivity of VO_2 in the metasurface system, the zeros associated with the FP mode and the QBIC move predominantly along the imaginary-frequency axis. Because the TCMT fitting yields a negligibly small and nearly constant coherent coupling κ_1 (Fig. 3e in the main text), the QBIC at $P = 121\,\mu$m can be approximated as a single-mode system, as described by Eq. S2. Inspection of Fig. 3d in the main text shows that, although the difference between the radiative and dissipative loss rates first increases sharply and then decreases slowly as the conductivity increases, it remains close to zero over the range 200S/m to 3×10^5S/m. Consequently, the zero $\omega_z = \omega_0 + i(\gamma_r - \gamma_d)$ only approaches, but does not readily cross, the real axis as the conductivity is increased. By contrast, at $P = 139\,\mu$m, where the system involves two coupled modes, increasing the VO_2 conductivity readily drives the zero across the real axis and into the upper half of the complex frequency plane. This striking behaviour originates from energy transfer between the coupled modes.

Section 8. The sinusoidal dependency of absorption on the substrate thickness

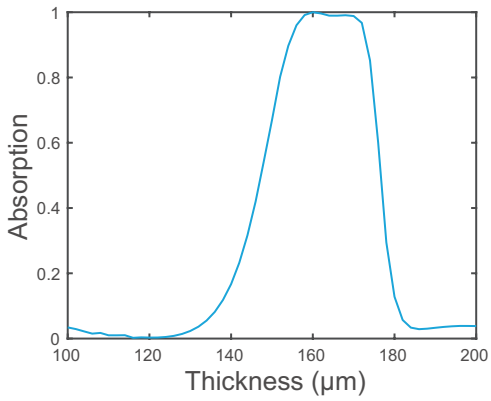

Fig. 7 Dependence of the system absorption on substrate thickness at 0.4347 THz.

Section 9. Spectral Fitting Process

By employing Eq. S4 derived in the previous section, we performed a fitting analysis of the spectral curves shown in Fig. 4b. As presented in Fig. 8, the fitting results are in excellent agreement with the numerical simulation data. Furthermore, the derivation of this single-port dual-mode TCMT model not only consolidates the theoretical framework for THz metasurface research, but also lays a foundation for extending the applicability of this theoretical formulation to a wider range of physical systems.

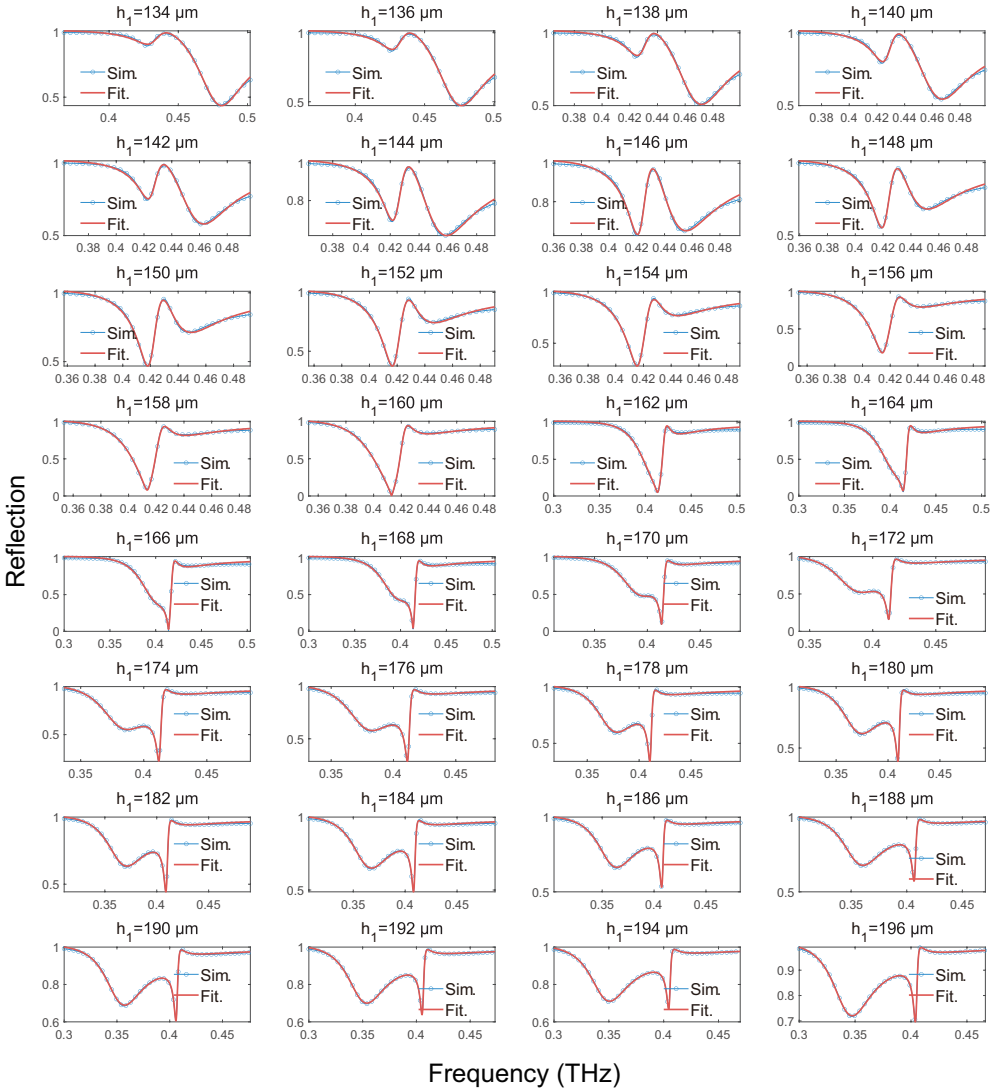

Fig. 8 Fitted curves for varying dielectric thicknesses at a conductivity of 9.2×10^4 S/m. The blue dotted lines represent the simulation data, while the red lines denote the fitted data.

Section 10. Calculation of mode Q-factors via TCMT

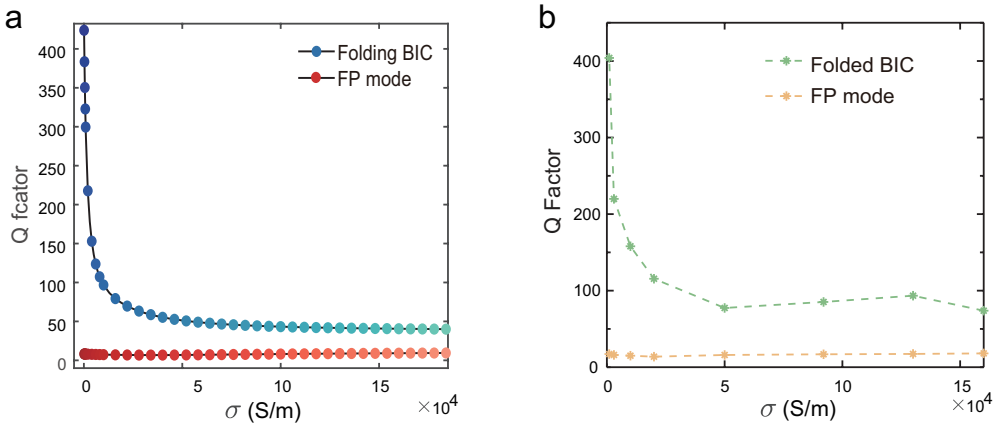

Fig. 9 Evolution of Q-factors for QBIC and FP modes as a function of conductivity based on TCMT.ă(a)ăSimulation results.ă**(b)**ăFitted results.

For the TCMT fitting of the curves shown in Fig. 4e of the main manuscript, we adopted Eq. S6 to derive the evolution of the Q-factors for both the FP mode and the BIC mode under conductivity modulation, with the period fixed to 139 μm and the substrate thickness fixed to $h = 160$ μm (Fig 9). As shown in Fig. 9a and b, the calculated results are in excellent agreement with the variation trends and orders of magnitude obtained from the numerical simulations, which verifies the validity of using the TCMT model to extract the Q-factors from the measured/simulated spectra.

Section 11. Absorptivity modulation depth

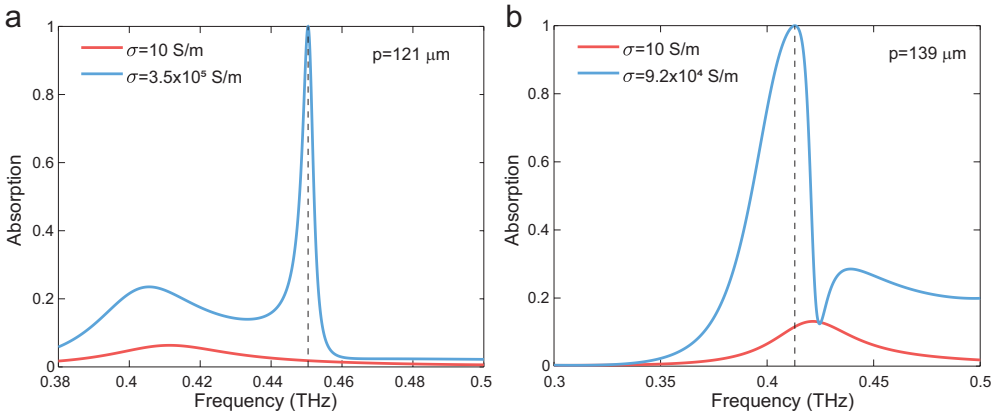

Fig. 10 **(a)**Absorptivity comparison at different conductivities for $P = 121$ μm. **(b)** Absorptivity comparison at different conductivities for $P = 139$ μm.

Section 12. Characterization of VO_2 conductivity

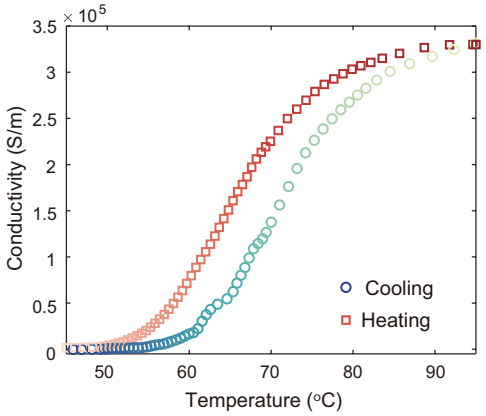

Fig. 11 Relationship of VO_2 conductivity as a function of temperature.

After depositing VO_2 on the sapphire substrate, THz transmission spectroscopy was performed using a temperature-controlled stage with gradual heating. First, the light intensity without the sample, $I_0(\omega)$, was measured as the reference background. The sample was then placed in the optical path to measure the transmitted intensity $I(\omega)$, with transmittance calculated as $T(\omega) = I(\omega)/I_0(\omega)$. Measurements were

repeated at different temperatures to record transmission spectra, with multiple scans averaged to improve signal-to-noise ratio. Sample thickness was verified using a profilometer or fabrication records. The real and imaginary parts of the permittivity extracted from transmittance were fitted to the Drude model to obtain the plasma frequency ω_p and electron relaxation rate γ'. The dielectric function of the Drude model is given by:

$$\varepsilon(\omega) = \varepsilon_\infty - \frac{\omega_p^2}{\omega^2 + j\omega\gamma'} \tag{S10}$$

where ε_∞ is the high-frequency dielectric constant, $\omega_p = \sqrt{ne^2/(m\varepsilon_0)}$ is the plasma frequency, n is the carrier concentration, e is the electron charge, m is the effective electron mass, and γ is the electron relaxation rate. For a sample with thickness d, the transmittance $T(\omega)$ is related to the complex refractive index $n'(\omega) = n'' + jk$ by:

$$T(\omega) = \frac{(1-R)^2 e^{-\alpha d}}{1 - R^2 e^{-2\alpha d}} \tag{S11}$$

where $R = \left|\frac{n'(\omega)-1}{n'(\omega)+1}\right|^2$ is the reflectance, $\alpha = \frac{4\pi k}{\lambda}$ is the absorption coefficient, k is the extinction coefficient, and $\varepsilon'' = 2n''k$. After simplifying $\alpha d \approx -\ln T(\omega)$, $k = \frac{\lambda}{4\pi d} \ln \frac{1}{T(\omega)}$ can be obtained.

Using the Kramers-Kronig transformation and combining with n'', we obtain $\varepsilon' = n''^2 - k^2$. Fitting these into the Drude model via nonlinear least squares yields ω_p and γ, allowing calculation of the VO_2 conductivity:

$$\sigma = \frac{ne^2}{m\gamma} = \frac{\omega_p^2 \varepsilon_0}{\gamma} \tag{S12}$$

where ε_0 is the vacuum permittivity. Finally, conductivity was calculated using the Eq. S12, yielding the relationship shown in Fig. 11.

Section 13. Sample fabrication

The sample was fabricated on a 160 μm-thick sapphire substrate (2 cm × 2 cm) using conventional lithography. First, a 200 nm-thick VO_2 layer was sputtered onto the double-polished sapphire substrate. A layer of photoresist (AZ1500) was then spin-coated over the VO_2 at 4000 rpm for 40 s, followed by a 2-minute soft bake on a hot plate at 90 °C. The predefined pattern on the photomask was transferred to the photoresist using an ultraviolet lithography system (ABM). Exposed photoresist was removed with positive photoresist developer for 17 s. Unprotected VO_2 regions were etched via reactive ion etching (RIE), and residual photoresist was cleaned in a cleanroom. Second, a new layer of photoresist (LOR10B) was spin-coated over the patterned substrate at 4000 rpm for 40 s, soft-baked at 130 °C for 2 minutes, and then coated with another layer of AZ1500 under the same parameters as the first step. The resonator rings were aligned and exposed, transferring the structure to the bilayer photoresist. After exposure, the bilayer photoresist was removed with positive photoresist developer for approximately 17 s. Gold (200 nm thick, same as the VO_2 layer) was deposited using physical vapor deposition (PVD), and remaining photoresist was stripped in N-methylpyrrolidone solution (NMP). Third, a layer of photoresist

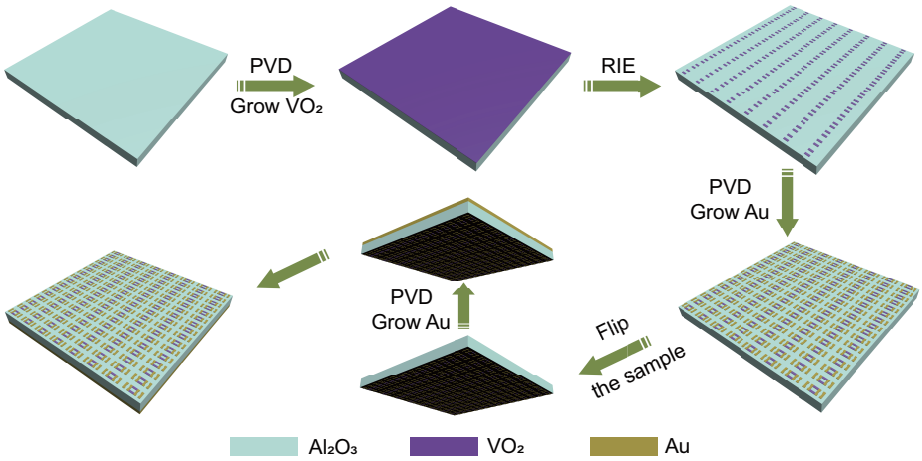

Fig. 12 Fabrication process of the THz metasurface.

(AZ10XT) was spin-coated on the front side (with resonator structures) to protect it during backside gold deposition. Another 200 nm-thick gold layer was deposited, and the sample was cleaned sequentially with acetone, ethanol, and water. The final sample and its microscopic image are shown in Fig. 12.

Section 14. Experimental spectral fitting and *Q*-factor evaluation

For the proposed metasurface with a period of $P = 121$ μm, we fitted the experimentally measured spectra at various temperatures using Eq. S4, yielding excellent agreement. As shown in Fig. 13, the circles denote the experimental spectral data, while the solid black lines represent the TCMT fitting results within the 0.35–0.45 THz range.

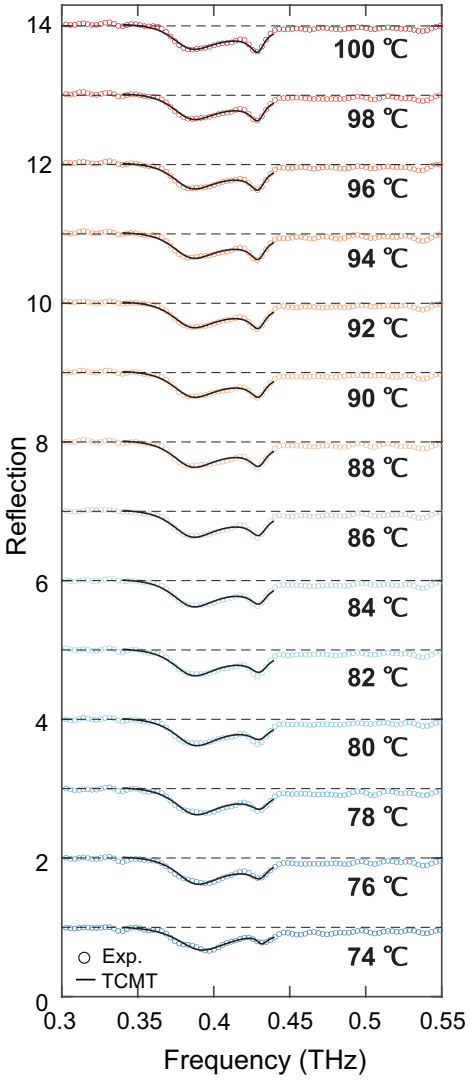

Fig. 13 Spectra fitted using TCMT and spectra obtained experimentally.

References

[1] Suh, W., Wang, Z. & Fan, S. Temporal coupled-mode theory and the presence of non-orthogonal modes in lossless multimode cavities. *IEEE Journal of Quantum Electronics* **40**, 1511–1518 (2004).

[2] Liu, W., Xu, S. & Lee, C. Ultracompact on-chip spectral shaping using pixelated nano-opto-electro-mechanical gratings. *Science* **389** (2025).